Reproducible graphene synthesis by oxygen-free chemical vapour deposition

https://doi.org/10.1038/s41586-024-07454-5

Received: 2 June 2023

Accepted: 22 April 2024

Published online: 29 May 2024



Check for updates

Jacob Amontree^{1,11}, Xingzhou Yan^{1,11}, Christopher S. DiMarco^{1,11}, Pierre L. Levesque^{2,3,4}, Tehseen Adel⁵, Jordan Pack⁶, Madisen Holbrook⁶, Christian Cupo¹, Zhiying Wang¹, Dihao Sun⁶, Adam J. Biacchi⁷, Charlezetta E. Wilson-Stokes^{5,8}, Kenji Watanabe⁹, Takashi Taniguchi⁹, Cory R. Dean⁶, Angela R. Hight Walker⁵, Katayun Barmak^{10⊠}, Richard Martel^{3,4™} & James Hone^{1™}

Chemical vapour deposition (CVD) synthesis of graphene on copper has been broadly adopted since the first demonstration of this process¹. However, widespread use of CVD-grown graphene for basic science and applications has been hindered by challenges with reproducibility² and quality³. Here we identify trace oxygen as a key factor determining the growth trajectory and quality for graphene grown by low-pressure CVD. Oxygen-free chemical vapour deposition (OF-CVD) synthesis is fast and highly reproducible, with kinetics that can be described by a compact model, whereas adding trace oxygen leads to suppressed nucleation and slower/incomplete growth. Oxygen affects graphene quality as assessed by surface contamination, emergence of the Raman D peak and decrease in electrical conductivity. Epitaxial graphene grown in oxygen-free conditions is contamination-free and shows no detectable D peak. After dry transfer and boron nitride encapsulation, it shows room-temperature electrical-transport behaviour close to that of exfoliated graphene. A graphite-gated device shows well-developed integer and fractional quantum Hall effects. By highlighting the importance of eliminating trace oxygen, this work provides guidance for future CVD system design and operation. The increased reproducibility and quality afforded by OF-CVD synthesis will broadly influence basic research and applications of graphene.

Since the first demonstration of CVD graphene growth on Cu (ref. 1). many advances have been made in the understanding, control and scaleup of the process. Seminal studies have provided understanding of the growth process through techniques such as isotopic labelling⁴ and in situ monitoring^{5,6} and have demonstrated control over key factors such as nucleation density^{7,8} and growth rate⁹. The initial demonstration of this process¹ has led to enormous interest as a route to scaled-up manufacturing, with subsequent advances including the development of roll-to-roll processing¹⁰, epitaxial growth on crystalline substrates (germanium¹¹ and Cu(111) (ref. 12)), in situ Cu deposition¹³ and control of folds/wrinkles¹³⁻¹⁵. Recent work has highlighted the accumulation of amorphous carbon on the graphene surface as a key factor affecting graphene performance^{3,16,17}.

In spite of these and many other advances, fundamental understanding and control of the CVD growth process is still lacking. For instance, although it has been experimentally established that the growth rate increases with CH₄ concentration and decreases with increasing H₂ concentration, there is not a well-accepted quantitative model of the growth kinetics that can be used to guide synthesis. Likewise, the fundamental processes influencing graphene quality are still unclear. More broadly, reproducibility of results remains a substantial challenge in the field², indicating the presence of hidden variables influencing graphene synthesis that are neither well controlled experimentally nor understood in theoretical models.

Here we will show that trace oxygen, which can enter by means of leaks, adsorption and the feed gases themselves, is the key hidden variable in low-pressure graphene CVD synthesis. Oxygen has been observed to play many different roles in graphene CVD synthesis $^{18-21}$. This work builds on previous findings that oxygen can etch graphene at parts-per-million (10^{-6}) concentrations²² and that graphene can be grown without H₂ in strictly oxygen-free conditions²³. Using a purpose-built low-pressure CVD reactor, we study the repeatability and growth kinetics of OF-CVD graphene synthesis; introduce trace oxygen to explain its effects on growth kinetics and graphene quality; and sensitively examine the quality of OF-CVD graphene by several techniques.

We find that OF-CVD growth is fast and highly repeatable. The dependence of growth rate on graphene coverage, temperature and methane/hydrogen partial pressure all show straightforward behaviour

Department of Mechanical Engineering, Columbia University, New York, NY, USA. 2Infinite Potential Laboratories, Waterloo, Ontario, Canada. 3Département de Chimie, Université de Montréal, Montréal, Quebec, Canada. Institut Courtois, Université de Montréal, Montréal, Quebec, Canada. Quebec, Canada Distinut Metrology Division, National Institute of Standards and Technology (NIST), Gaithersburg, MD, USA. 6Department of Physics, Columbia University, New York, NY, USA. 7Nanoscale Device Characterization Division, National Institute of Standards and Technology (NIST), Gaithersburg, MD, USA. Bepartment of Mechanical Engineering, Howard University, Washington, DC, USA. Research Center for Functional Materials, National Institute for Materials Science, Tsukuba, Japan. 10 Department of Applied Physics and Applied Mathematics, Columbia University, New York, NY, USA. 11 These authors contributed equally: Jacob Amontree, Xingzhou Yan, Christopher S. DiMarco. [™]e-mail: kb2612@columbia.edu: r.martel@umontreal.ca: ih2228@columbia.edu

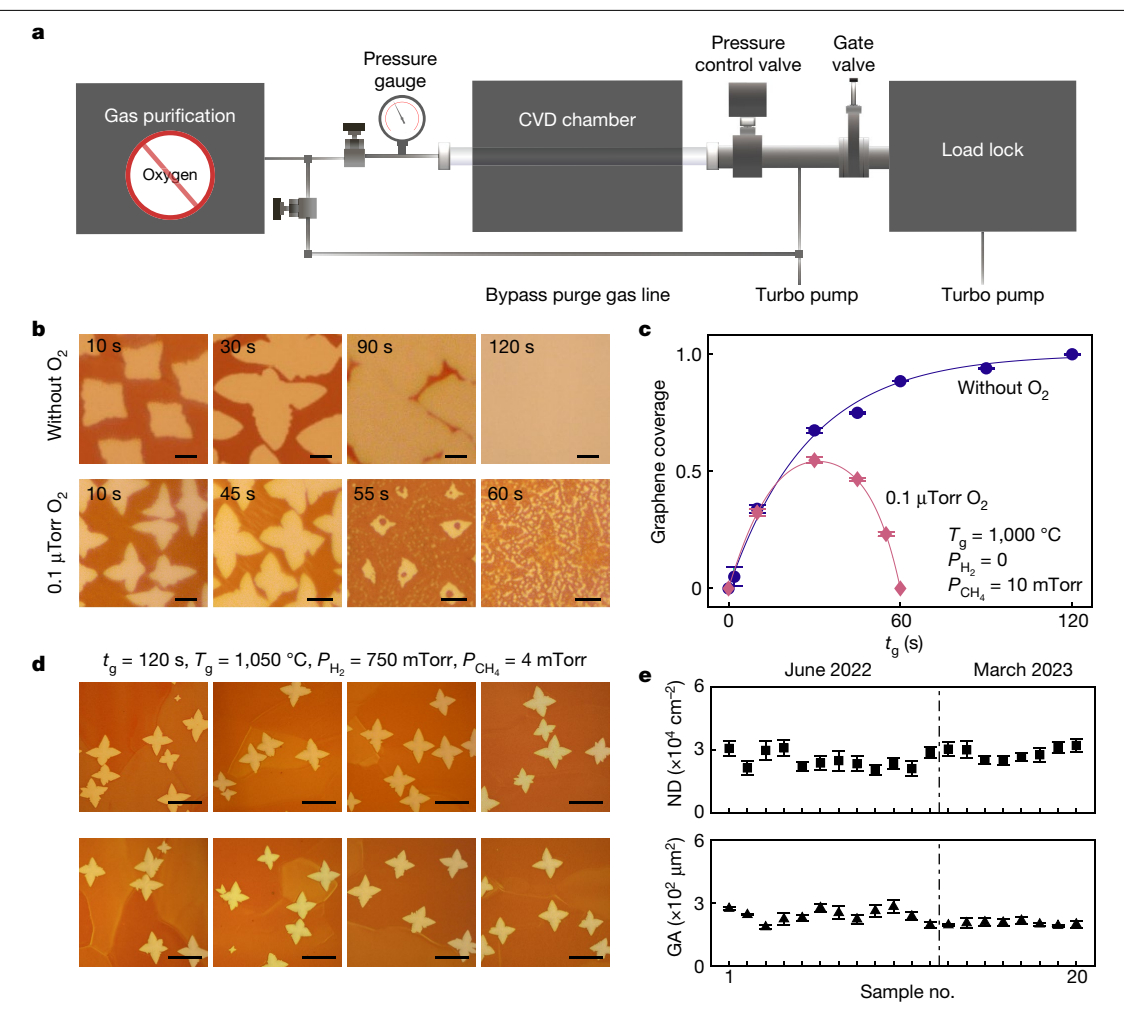


Fig. 1 | OF-CVD system design, influence of trace oxygen and high reproducibility. a, System overview highlighting key components to reduce oxidizing impurities. b, Optical images of grain evolution for hydrogen-free graphene growth with $P_{\text{CH}_a} = 10 \text{ mTorr}$, for $t_g = 10 \text{ s}$, 30 s, 90 s and 120 s. Top row, oxygen-free growth; bottom row, growth with $P_{0} = 0.1 \,\mu\text{Torr.}$ Scale bars, 5 $\,\mu\text{m.}$

 \mathbf{c} , Graphene coverage versus t_a with and without trace oxygen. \mathbf{d} , Representative images of graphene grains for eight distinct synthesis runs. Scale bars, 30 µm. e, Average graphene grain nucleation density (ND) and grain area (GA) versus sample number. Error bars indicate the standard deviation (1σ , n = 10).

that can be quantitatively captured by compact models. We confirm the role of oxygen as a hidden variable in two ways. First, we demonstrate that trace oxygen strongly modifies growth kinetics and outcomes in both H₂-free and H₂-rich conditions. Second, we discover a link between trace oxygen and accumulation of amorphous carbon, with clear impact on electrical conductivity.

OF-CVD graphene shows high quality as assessed by Raman spectroscopy, with no evidence of surface contamination in scanning probe microscopy. Electrical devices on SiO₂ show uniformly high mobility and hexagonal boron nitride (h-BN)-encapsulated devices show performance exceeding all previous reports for CVD graphene and rivalling that of exfoliated graphene. In a graphite-gated device, we observe fully developed fractional quantum Hall effect at B = 15 T.

OF-CVD system design, effect of trace O₂ and reproducibility

Figure 1a shows a schematic of the CVD reactor used in this study. The system is based on the hot-wall design most commonly used in laboratory research and operates at low pressure to best maintain system cleanliness. High vacuum is achieved by turbomolecular pumping and flows of CH₄, H₂, O₂ and Ar are controlled by mass flow controllers. All gas lines are electropolished stainless steel with helium-leak-checked metal fittings. Because research-grade gases commonly contain oxygen impurities in the ppm range, we use ultra-large-scale integration

(ULSI)-grade gas (6N purity) and purifiers that remove impurities (H₂O, O_2 , CO_2 , CO) to <100 parts-per-trillion (10^{-12}) levels. Each gas line is purged before being turned on to avoid transient pressure spikes (which can cause uncontrolled graphene nucleation in the case of CH₄; Supplementary Fig. 9). A turbo-pumped load lock enables sample exchange without exposing the system to air. Trace gas analysis verifies that the partial pressure of oxygen-containing contaminants (H₂O, O₂, CO₂, CO) is less than 1 µTorr (Supplementary Fig. 12). An exhaust throttle valve is used to maintain a specified total pressure in the synthesis chamber. Partial pressures of the constituent gases $(P_{CH_4}, P_{H_2}, P_{O_2} \text{ and } P_{Ar})$ are calculated from flow rate ratios (Supplementary Information equation (S1)). Although the SI unit for pressure is pascal (Pa), herein, Torr will be the unit used, as it is common practice of the field; 1 Torr = 133.32236842 Pa. A complete schematic of the CVD system design can be found in Supplementary Fig. 1.

Graphene CVD synthesis is performed using the typical process in which the Cu substrate is heated in a hydrogen-rich atmosphere to the growth temperature $T_g \approx 1,000$ °C, followed by a growth phase with CH_4 for duration t_g and then cooling to room temperature. Details of the growth process are given in Methods and growth parameters for each experiment are summarized in Supplementary Table 1. For initial studies (Figs. 1-3), we use Cu foil (Alfa Aesar 46365 Cu foil, 0.025 mm thick, 99.8%) that is electrochemically polished to sub-nanometre

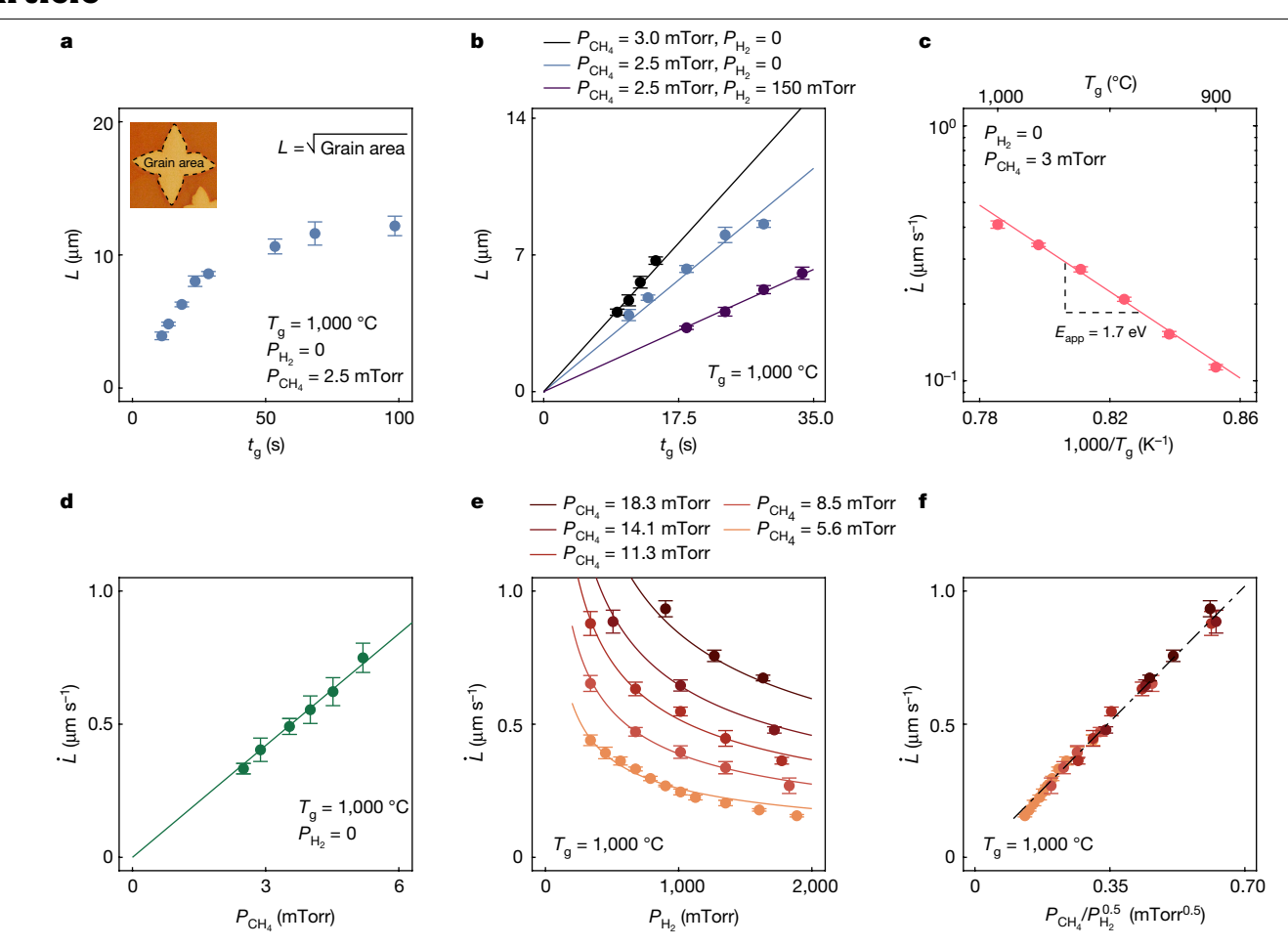


Fig. 2 | **Kinetics of graphene grain growth.** Each data point in this figure represents a distinct graphene sample, with relevant parameters determined by image analysis, and error bars indicate the standard deviation $(1\sigma, n = 10)$. Growth conditions are as noted in each panel. **a**, Lateral grain size $L = \sqrt{\text{Grain area}}$ versus growth duration, t_{gr} with $P_{\text{H}} = 0$. **b**, L shows linear dependence on t_{gr} at early

growth stage. \mathbf{c} , Grain growth rate \dot{L} versus T_{g} . Solid line shows exponential fit with an activation energy of $E_{\mathrm{app}}=1.7\pm0.06$ eV. \mathbf{d} , \dot{L} versus $P_{\mathrm{CH_4}}$. Solid line is linear fit. \mathbf{e} , \dot{L} versus $P_{\mathrm{H_2}}$ for $P_{\mathrm{CH_4}}=5.6$ mTorr, 8.5 mTorr, 11.3 mTorr, 14.1 mTorr and 18.3 mTorr. \mathbf{f} , \dot{L} versus $P_{\mathrm{CH_4}}/P_{\mathrm{H_2}^3}^{0.3}$. Dashed line is linear fit.

roughness, which reduces the thickness from 25 μ m to 15 μ m and removes surface impurities. A typical growth substrate is 4 mm \times 2 mm, which is pre-annealed in H $_2$ to increase grain size (hundreds of μ m) with predominantly (100) texture (Supplementary Fig. 21). To visualize graphene domains after growth, the foil is heated in air at 200 °C for 1 min to oxidize exposed Cu, such that areas with graphene appear shiny against a dull orange background.

The top row of Fig. 1b shows optical microscope images of substrates after synthesis of graphene in the absence of H_2 . Isolated grains with approximately 20 μ m separation appear at t_g = 10 s and then grow and merge to form a continuous film with no detectable pinholes at t_g = 120 s. The fourfold grain symmetry matches that of the underlying Cu(100), indicating that growth is supply-limited rather than attachment-limited²⁴.

With trace oxygen ($P_{\rm O_2}/P_{\rm CH_4}=10^{-6}$) added during the growth stage, grains initially grow but then shrink and disappear at higher $t_{\rm g}$ (Fig. 1b, bottom row). To quantify the growth trajectory in each case, we used optical image processing (Supplementary Fig. 3) to calculate the fractional graphene coverage for each sample, with the results plotted in Fig. 1c. Without oxygen, coverage increases smoothly with $t_{\rm g}$; with trace oxygen, initial growth is similar but coverage subsequently decreases and the graphene disappears. These findings support the conclusions of earlier work^{22,23} and extend it by demonstrating the speed of OF-CVD growth and growth/etching trajectory in the presence of trace oxygen.

To test the reproducibility of OF-CVD, we synthesized graphene for $t_{\rm g}=120~{\rm s}$ using a recipe that achieves well-separated grains and measured the average nucleation density and grain area over a large region $(1~{\rm mm}^2~{\rm to}~2~{\rm mm}^2)$. This process was repeated 12 times initially and then eight more times after 9 months. Figure 1d shows optical images of the resulting graphene grains for eight iterations with images from all 20 in Supplementary Fig. 4. As shown in Fig. 1e, the nucleation density and grain area are remarkably consistent, with a coefficient of variation of 13%, and are not affected by ambient conditions.

Kinetics of grain growth

The high speed and reproducibility of OF-CVD synthesis allows us to study growth kinetics by tracking grain morphology for several samples across which a given parameter (t_g , T_g , P_{CH_4} , P_{H_2}) is adjusted. As discussed above, we find that OF-CVD growth begins with rapid grain nucleation, followed by grain expansion to achieve complete coverage. The number of nuclei does not increase with t_g (Supplementary Fig. 6). Figure 2a illustrates a typical trajectory for grain growth: the grain size $L \equiv \sqrt{GA}$ initially increases rapidly with t_g ; grain growth slows as the film approaches full coverage, at which point $L = 1/\sqrt{ND}$ (images in Supplementary Fig. 7). For simplicity, here we focus on early-stage growth, in which grains are well separated. As shown in Fig. 2b for three different growth conditions, L initially increases linearly with t_g . Therefore, only a single sample is required to determine the grain growth rate $L = L/t_g$ for each point in Fig. 2c–f.

As shown in Fig. 2c, \dot{L} shows activated temperature dependence with characteristic energy (apparent activation energy) of $E_{app} = 1.7 \pm 0.06$ eV. At fixed T_g , \dot{L} shows linear dependence on P_{CH_4} (Fig. 2d). Together with the fourfold grain shape, these findings support a picture in which the growth rate is limited by the supply of carbon 25,26, which is in turn governed by catalytic dehydrogenation of CH₄ at the Cu surface.

We next explore how \dot{L} varies with $P_{\rm H_2}$ in the regime in which $P_{\rm H_2} \gg P_{\rm CH_4}$. As shown in Fig. 2e, \vec{L} decreases with increasing $P_{\rm H_2}$, with $\vec{L} \propto P_{\rm H_2}^{-0.5}$ (solid lines). The $P_{\rm H_2}^{-0.5}$ dependence indicates that at least one of the steps in the CH₄ dehydrogenation process is in equilibrium. Therefore, we assume that \dot{L} is determined by the surface density of methyl species, [CH₃], which is in turn determined by the (quasi-equilibrium) dissociative adsorption of CH₄ and H₂. A simple model for the reaction kinetics (details and discussion of underlying assumptions in Supplementary Information section 9) gives

$$\dot{L} \propto [\text{CH}_3] \propto \frac{K_{\text{eq}}^{\text{CH}_4}}{K_{\text{eq}}^{\text{H}_2}} \cdot \frac{P_{\text{CH}_4}}{P_{\text{H}_3}^{0.5}},$$
 (1)

in which $\textit{K}_{eq}^{\text{CH}_4}$ and $\textit{K}_{eq}^{\text{H}_2}$ are equilibrium constants for the CH4 and H2 dissociation reactions, respectively. Figure 2f confirms that the data in Fig. 2e collapse onto a single linear function of $P_{\rm CH_a}/P_{\rm H_2}^{0.5}$, consistent with this model. We note that E_{app} increases in the presence of H_2 (Supplementary Fig. 11), consistent with modification of the equilibrium of the intermediate reactions²⁷.

Effect of trace O₂ on growth and quality in typical CVD conditions

Trace oxygen plays a key role in controlling growth outcomes even under typical (hydrogen-rich) CVD conditions, in which the reducing atmosphere should offset etching by oxygen. In Fig. 3, we grow graphene with $P_{\rm H_2}$ = 150 – 500 mTorr and $P_{\rm CH_4}$ = 3 – 10 mTorr, which are typical ranges for studies reported in the literature, and flow oxygen for the entire synthesis process (versus only the growth stage as in Fig. 1) to mimic a CVD system with a small leak or other oxygen contamination.

Figure 3a shows graphene coverage versus t_g for $P_{O_2} = 0 \mu Torr$, 1 μTorr, 4 μTorr and 8 μTorr (solid lines are guides to the eye). Without oxygen, complete coverage is achieved in 12 min, following a similar trajectory as in Fig. 2a, but with a slower rate owing to the addition of hydrogen (Supplementary Fig. 14a-c). Adding 1 uTorr of oxygen slows growth by roughly a factor of 5, but full coverage is still achieved (Supplementary Fig. 14d-f). For P_{O_2} = 4 μ Torr and 8 μ Torr, etching takes over at large t_g and full coverage is never achieved (Supplementary Fig. 14g-i). The onset of growth is also delayed. This delay does not occur if oxygen is introduced only with the methane (Supplementary Fig. 13) and therefore probably reflects suppressed nucleation when the Cu surface is oxidized, consistent with previous findings 18,20. Thus, although hydrogen does increase the threshold for etching, trace oxygen nevertheless strongly modifies both nucleation and growth rate and can prevent growth of complete films.

Also, we find that trace oxygen plays an as yet unidentified role in reducing graphene quality even when complete coverage is achieved. To study the effect of oxygen on quality, we synthesized four samples with identical $t_g = 120$ min and varying P_{O_2} . For these samples, we assess three measures of quality: surface cleanliness, using atomic force microscopy (AFM) and X-ray photoemission spectroscopy (XPS) (Fig. 3b); lattice defects, using Raman spectroscopy (Fig. 3c); and electronic transport (Fig. 3d).

The top row of Fig. 3b shows AFM images of two of these samples, with further images in Supplementary Fig. 16. Within an individual Cu terrace, the sample grown with $P_{O_3} = 0 \mu \text{Torr}$ is flat, whereas the sample grown with $P_{O_2} = 1.32 \mu \text{Torr shows a thin layer of contamination,}$ which can be further visualized by selective adsorption of Au (ref. 3) (Supplementary Fig. 17). XPS spectra (Fig. 3b, bottom row) show a large increase in the peak at 285.2 eV, indicative of sp³-bonded carbon, for the sample with O₂. We can thus conclude that the presence of trace oxygen during CVD growth leads to accumulation of amorphous carbon, which has recently been identified as a key indicator of graphene quality^{3,28}. The mechanism for this is not clear, although control experiments indicate that the contamination is not a strictly gas phase reaction (Supplementary Fig. 19).

Figure 3c shows representative Raman spectra from each of the four samples after wet transfer to SiO₂, with an expanded view of the D-peak region shown in the inset. The D peak is negligible for $P_{O_{1}} = 0 \mu \text{Torr}$ and grows with increasing $P_{O_{a}}$, whereas the 2D peak shrinks; both trends are indicative of the appearance of defects in the graphene lattice. The D-peak signal shows a striated pattern (inset) that mirrors steps in the Cu (further Raman mapping data in Supplementary Fig. 18).

For electrical-transport measurements, we used wet transfer to assemble h-BN-encapsulated devices from each of the four graphene films. Figure 3d shows the room-temperature electrical conductivity (left panel) and Hall mobility (right panel) as a function of electron density for all four samples. At fixed density, the conductivity and mobility decrease with increasing P_{0} , confirming that trace oxygen degrades graphene performance in a regime that is broadly relevant to applications.

High-quality OF-CVD graphene

We assess the quality of OF-CVD graphene using a combination of scanned probe imaging, Raman spectroscopy and electrical-transport measurements. Because CVD growth on Cu foil leads to wrinkles and folds that can complicate interpretation, for these experiments, we grow graphene on sapphire(0001)-supported Cu(111) films (Supplementary Fig. 22), on which growth is epitaxial and wrinkles are suppressed¹². (Growth recipes are the same as for growth on foil; see Methods and Supplementary Information). Graphene was transferred from the growth substrate by wet transfer after etching the Cu or by dry transfer after oxidizing the Cu surface^{29,30} (Supplementary Fig. 25).

Figure 4a shows an AFM topography image of a graphene/Cu(111) sample. Cu atomic steps are clearly visible and we find no evidence of amorphous carbon contamination¹⁶ (further AFM data in Supplementary Fig. 23). Imaging by scanning tunnelling microscopy (STM) clearly resolves the graphene atomic lattice (Fig. 4b, inset); a larger-area STM scan (Fig. 4b) shows atomically flat Cu terraces, as well as a superlattice with approximately 10 nm period arising from the moiré pattern between the Cu and graphene. No amorphous carbon is observed over several STM images (Supplementary Fig. 24). Thus we can conclude that the OF-CVD graphene is free of surface contamination.

To measure the intrinsic Raman spectrum of OF-CVD graphene in the absence of substrate effects, we create a suspended membrane by wet transfer to a holey carbon grid. The measured spectrum in Fig. 4c shows high 2D/G peak area ratio $(A_{2D}/A_G \approx 13.75)$, indicative of high electronic quality. No D peak is visible. On the basis of the noise level (inset), we estimate that $A_D/A_C \lesssim 0.01$. This implies defect spacing of $L_D \gtrsim 120$ nm (ref. 31), that is, point defect density less than 2.2×10^9 cm⁻². Raman spectra and maps on three other substrates (as-grown on Cu(111), on Si/SiO₂ and encapsulated in h-BN) (Supplementary Fig. 26 and Supplementary Table 2) also indicate high quality and uniformity. No grain boundaries are visible, consistent with epitaxial growth.

We next examine electrical-transport properties of the OF-CVD graphene. An array of 50 devices created by wet transfer to Si⁺⁺/SiO₂ shows high uniformity and performance on par with previous reports for ultra-clean graphene (Supplementary Fig. 27). For more precise assessment of the intrinsic electrical-transport performance, we study a smaller number of dry-transferred devices that are encapsulated within h-BN to reduce environmental effects. Figure 4d,e shows the average and spread of room-temperature electrical conductivity (σ) versus electron density (n) and Hall mobility (μ) versus electron density (n) for three OF-CVD-grown samples and three samples created

Article

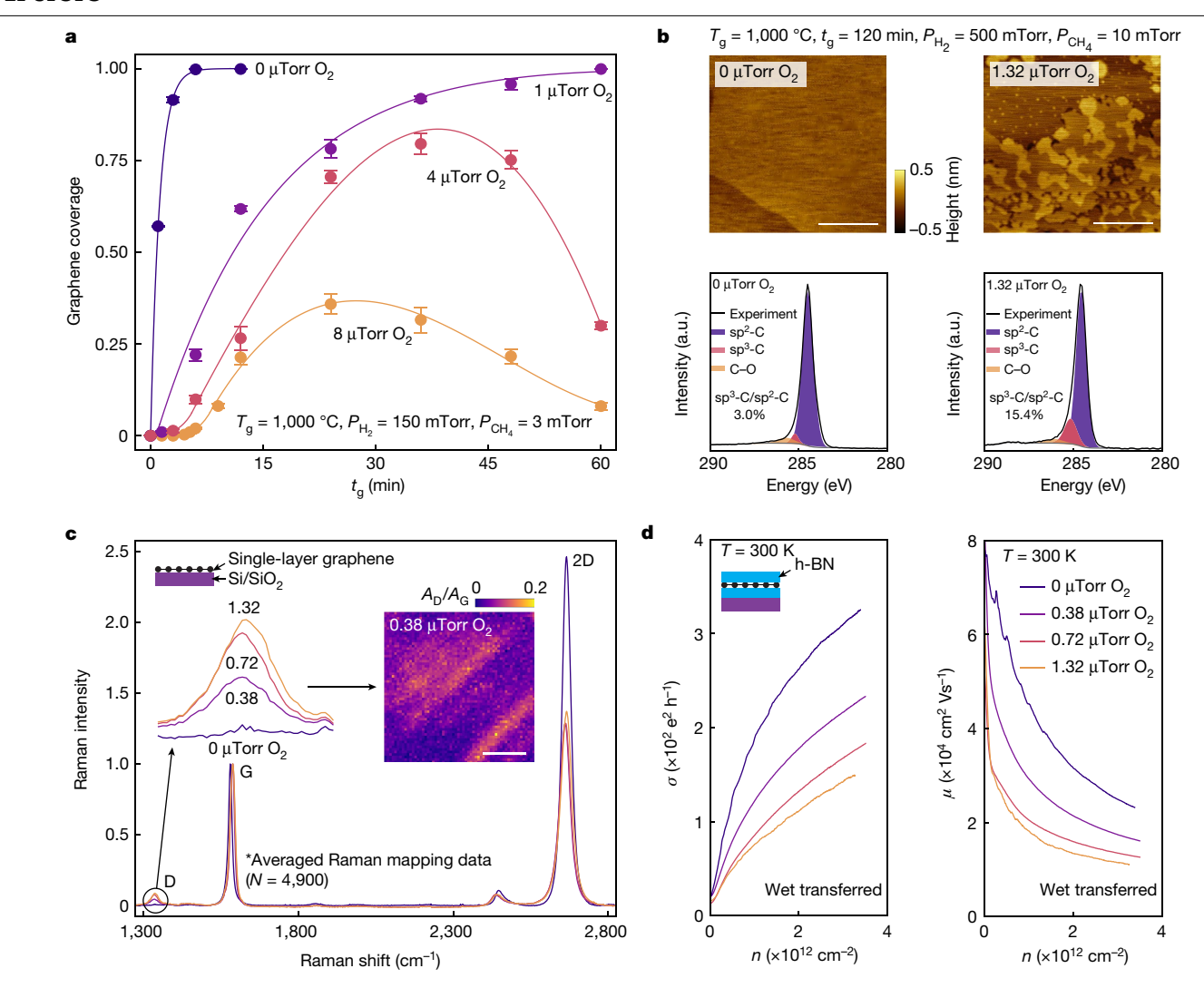


Fig. 3 | Effects of trace O_2 on graphene growth under typical (hydrogen-rich) CVD conditions. a, Graphene coverage as a function of $t_{\rm g}$ for varied $P_{\rm O_2}$ as shown. Each data point represents a distinct graphene sample, with error bars indicating the standard deviation (1σ , n=10). b, Surface cleanliness characterization of graphene synthesized with trace O_2 . Top row, AFM height topography of the Gr/Cu surface grown with O_2 -free and $P_{\rm O_2}=1.32~\mu$ Torr, respectively. The Gr/Cu surface with O_2 -free synthesis is free of contamination, whereas synthesis using $P_{\rm O_2}=1.32~\mu$ Torr has widespread amorphous carbon residue. Scale bars, $100~\rm nm$. Bottom row, XPS analysis of graphene on copper immediately after growth with O_2 -free and $P_{\rm O_2}=1.32~\mu$ Torr, respectively. The ratio of sp³-C/sp²-C increased

by five times with synthesis using $P_{\rm O_2}$ =1.32 μ Torr compared with O_2 -free conditions. a.u., arbitrary units. **c**, Averaged Raman spectra of Gr/SiO₂ samples synthesized with varied $P_{\rm O_2}$. Raman characterization was collected with 532 nm excitation (1 mW, 1 s, one accumulation) at 0.1 μ m step size (N=4,900). Left inset, evolution of the D band with increased $P_{\rm O_2}$ introduced during $t_{\rm g}$. Right inset, $A_{\rm D}/A_{\rm G}$ Raman mapping of Gr/SiO₂ samples synthesized with $P_{\rm O_2}$ =0.38 μ Torr. Scale bar, 2 μ m. **d**, Room-temperature conductance (left) and Hall mobility (right) as a function of carrier density (n) of four graphene h-BN-encapsulated CVD graphene devices, in which varied $P_{\rm O_2}$ was introduced during $t_{\rm g}$.

from exfoliated graphene, whose performance closely matches previous reports (that is, mobility near the theoretical phonon limit for $n > 2 \times 10^{12} \, \mathrm{cm^{-2}})^{32}$. The OF-CVD graphene shows conductivity and mobility that is extremely close to that of the exfoliated samples. At low temperature (T = 1.6 K), the OF-CVD graphene shows ballistic transport over the approximately 5 μ m sample size for $n > 6 \times 10^{11} \, \mathrm{cm^{-2}}$ (Supplementary Fig. 28).

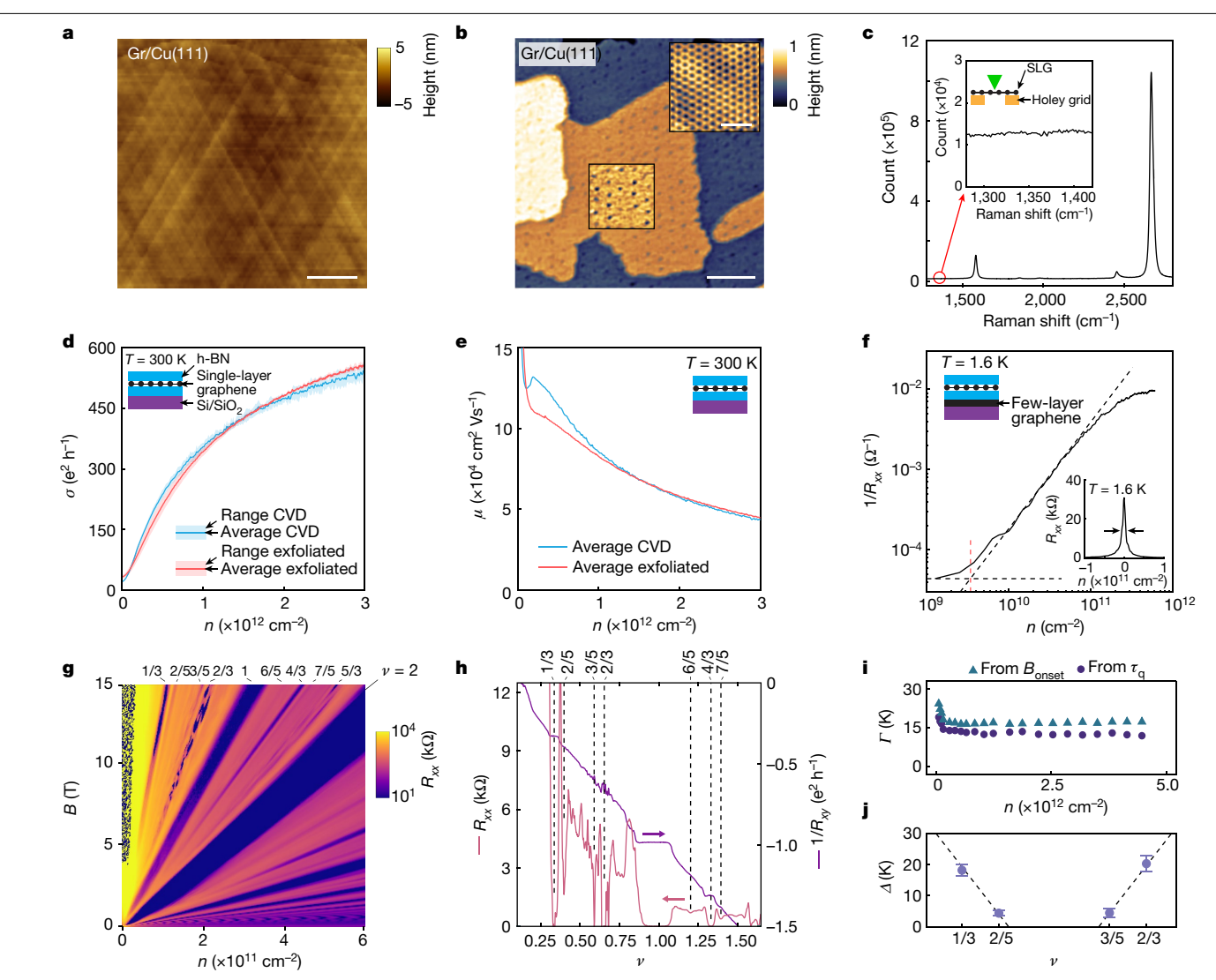
For low-temperature studies, the same dry-assembly method was used to create a sample with a graphite back gate to screen charge disorder from the SiO₂. A double-log plot σ versus n (Fig. 4f) indicates a residual carrier density of 3.5×10^9 cm⁻². The narrow (8×10^9 cm⁻²) Dirac peak (inset) also reflects low charge disorder. Figure 4g–j summarizes the low-temperature magnetotransport behaviour of this device. Figure 4g shows the Landau fan obtained by plotting the longitudinal resistance (R_{xx}) as a function of n and applied magnetic field (B). Well-developed integer quantum Hall states with $R_{xx} = 0$ appear below about 0.5 T, indicative of very high quality. Moreover, numerous

fractional states appear at higher fields. Figure 4h shows a line plot of R_{xx} and Hall conductance $(1/R_{xy})$ as a function of filling fraction (v) at B=15 T. Fully developed states with $R_{xx}=0$ and clear plateaus in $1/R_{xy}$ are seen for $v=\frac{1}{3},\frac{2}{5}$ and $\frac{4}{5}$ and more states are seen for $v=\frac{2}{5},\frac{3}{5},\frac{6}{5}$ and $\frac{7}{5}$.

For a more quantitative measure of quality, we used Shubnikov-de Haas (SdH) oscillations to calculate the Landau-level broadening (Γ) (Fig. 4i). Both the envelope of the SdH oscillations (Dingle plot) (Supplementary Fig. 31) and the onset of oscillations yield $\Gamma \simeq 15$ K over a wide range of densities. As a second measure of broadening, we measure $R_{xx}(T)$ to determine the activation gaps for four fractional states (Fig. 4j and Supplementary Fig. 30). The measured gaps are consistent with the small value of Γ .

Discussion

These results reinforce conclusions of earlier work demonstrating etching of graphene by trace oxygen²², and hydrogen-free growth in its



 $\textbf{Fig. 4} | \textbf{High-quality OF-CVD graphene.} \ Continuous films are grown on$ sapphire(0001)-supported Cu(111) films. a, AFM topography of the Gr/Cu surface showing flat surface with few folds/wrinkles and no detectable surface contamination. Diagonal lines are Cu atomic steps. Scale bar, 1 µm. b, STM image of graphene surface. Upper-right inset shows the atomic-resolution map of the Gr honeycomb lattice. Centre inset shows the Cu/Gr moiré pattern. Scale bars, 20 nm (main), 1 nm (inset). c, Raman spectrum of suspended graphene collected with 532 nm excitation (0.7 mW power, 120 s and 15 accumulations). Inset shows the lack of an identifiable D peak. Data in d and e refer to the h-BN-encapsulated CVD graphene sample transferred using the polymer-free dry transfer method with Si^{++}/SiO_2 gating. **d**, Room-temperature conductivity (σ) versus density for three CVD and exfoliated graphene devices. \mathbf{e} , Room-temperature mobility (μ)

versus density for three CVD and exfoliated graphene devices. f-j refer to the h-BN-encapsulated CVD graphene sample transferred using the polymer-free method with few-layer-graphene gating. f, Low-temperature (1.6 K) inverse four-terminal resistance $(1/R_{xx})$ versus density. The intercept of two lines following the regimes of constant slope provides an estimate of the residual charge-carrier fluctuations $n^* = 3.5 \times 10^9 \text{ cm}^{-2}$. **g**, Landau fan diagram of the longitudinal resistance, R_{xx} , as a function of density and magnetic field. \mathbf{h} , R_{xx} and $1/R_{xy}$ measured at 15 T for y < 2. R_{xx} shows minima or zeros at the labelled filling fractions. i, Landau-level broadening Γ , extracted from quantum lifetime $\tau_{\rm q}$ (circles) and the onset of SdH oscillations (triangles) versus carrier density n. j, Activation gaps for the observed fractional quantum Hall states in the N=0 $level \, as \, a \, function \, of \, filling \, fraction. \, SLG, single-layer \, graphene. \,$

absence²³. Going beyond the previous work, we demonstrate the time progression of grain growth and etching, establish that eliminating oxygen leads to high reproducibility and show that oxygen strongly modifies growth kinetics and outcomes even under hydrogen-rich conditions.

We further establish that key aspects of early-stage grain-growth kinetics can be captured by a compact model. This result will guide continuing efforts to comprehensively understand graphene growth kinetics, based on multiscale and multiphysics modelling of key steps such as catalytic CH₄ dehydrogenation, surface diffusion of carbon and attachment at the grain edge. Moreover, this compact model is of great practical utility because it quantitatively predicts how changing methane and hydrogen partial pressures will modify the growth rate.

Thus, this work establishes that removal of trace oxygen provides both reproducibility under fixed conditions and predictability of system response when parameters are changed.

An entirely new finding in this work is the clear experimental link between trace oxygen and amorphous carbon contamination, which has attracted considerable recent attention as a key determinant of graphene quality. Although numerous recent publications have explored methods to minimize or remove amorphous carbon, none has identified oxygen as an underlying factor. The microscopic mechanism by which this occurs is still unclear and will be explored in future investigations.

The OF-CVD graphene quality achieved here matches or exceeds that in previous reports for CVD graphene. The surface cleanliness

Article

seen in scanned probe imaging (Fig. 4a,b) matches previous reports for ultra-clean graphene using a copper foam technique³. The room-temperature mobility of the h-BN-encapsulated samples (Fig. 4e) exceeds that of previous reports for CVD graphene^{30,33} by 10–13%; this margin exceeds the difference between the mobilities OF-CVD and exfoliated graphene (Supplementary Fig. 32a,b). The low-T charge disorder and Landau-level broadening (Fig. 4i,j) are the smallest reported for CVD graphene and comparable with the best results for exfoliated graphene^{34,35}. The fractional quantum Hall states observed here are fully developed (with $\sigma_{xx} = 0$) at B = 15 T, whereas previous reports do not achieve fully developed states even at B = 35 T (ref. 30) (Supplementary Fig. 32c).

The finding that trace oxygen controls graphene growth and quality provides valuable insight into the challenges of reproducibility and quality in graphene CVD synthesis. In a conventional CVD system, oxidizing impurities can enter in a variety of ways (for example, impurities in gas feedstock, leaks, adsorbates) with concentration that varies over time, leading in turn to variable results. As one example, we have seen that accumulation of copper (which can act as either a sink or a source for O_2) on the quartz reactor tube modifies sensitivity to trace oxygen (Supplementary Fig. 15).

High reproducibility will allow for systematic investigation of other factors beyond those studied here. For example, we observed that gas pressure also controls nucleation density (Supplementary Fig. 8a,b), and it should be possible to develop quantitative understanding of this process in future work. We have used this control to grow large-grain $(L > 300 \mu m)$ OF-CVD graphene on Cu foil (Supplementary Fig. 8c) (it should be possible to achieve millimetre-scale grains by further suppressing nucleation³⁶). Likewise, with removal of trace oxygen as a hidden variable, it will be possible to better understand how the copper foil (grain orientation, impurities etc.) affects growth (Supplementary Fig. 20). Finally, we find that oxidizing the Cu substrate after OF-CVD graphene growth requires elevated temperatures (see Methods) rather than occurring under ambient conditions, as in previous work³⁷. This observation is consistent with recent reports³⁸. Likewise, OF-CVD graphene has proved to be more difficult to transfer using electrochemical delamination. This indicates that defects and/or contaminants influence graphene transfer, which may explain why transfer of CVD graphene also suffers from lack of reproducibility².

OF-CVD graphene synthesis provides the reproducibility and quality needed for both fundamental research and applications. Adoption of this method by groups in academic institutions and industry (together with development of scalable transfer techniques) will affect both fundamental research requiring ultra-high performance and applications in sensing, electronics and optoelectronics. In industrial settings, reduced need for hydrogen will reduce the need for costly safety measures. To demonstrate the transferability of these findings, we were able to achieve closely matching results in a second (hot-wall, low-pressure) OF-CVD system in a different location and with a different design (Supplementary Fig. 5). Further work will be needed to establish transferability to cold-wall and atmospheric-pressure CVD systems.

Online content

Any methods, additional references, Nature Portfolio reporting summaries, source data, extended data, supplementary information, acknowledgements, peer review information; details of author contributions and competing interests; and statements of data and code availability are available at https://doi.org/10.1038/s41586-024-07454-5.

- Li, X. et al. Large-area synthesis of high-quality and uniform graphene films on copper foils. Science 324, 1312–1314 (2009).
- Bøggild, P. Research on scalable graphene faces a reproducibility gap. Nat. Commun. 14, 1126 (2023).
- 3. Lin, L. et al. Towards super-clean graphene. Nat. Commun. 10, 1912 (2019).

- Li, X., Cai, W., Colombo, L. & Ruoff, R. S. Evolution of graphene growth on Ni and Cu by carbon isotope labeling. Nano Lett. 9, 4268–4272 (2009).
- Kidambi, P. R. et al. Observing graphene grow: catalyst-graphene interactions during scalable graphene growth on polycrystalline copper. Nano Lett. 13, 4769–4778 (2013).
- Wang, Z. J. et al. Direct observation of graphene growth and associated copper substrate dynamics by in situ scanning electron microscopy. ACS Nano 9, 1506-1519 (2015).
- Braeuninger-Weimer, P., Brennan, B., Pollard, A. J. & Hofmann, S. Understanding and controlling Cu-catalyzed graphene nucleation: the role of impurities, roughness, and oxygen scavenging. Chem. Mater. 28, 8905–8915 (2016).
- Wang, J., Park, J. H., Lu, A. Y. & Kong, J. Electrical control of chemical vapor deposition of graphene. J. Am. Chem. Soc. 144, 22925–22932 (2022).
- Xu, X. et al. Ultrafast growth of single-crystal graphene assisted by a continuous oxygen supply. Nat. Nanotechnol. 11, 930–935 (2016).
- Polsen, E. S., McNerny, D. Q., Viswanath, B., Pattinson, S. W. & John Hart, A. High-speed roll-to-roll manufacturing of graphene using a concentric tube CVD reactor. Sci. Rep. 5, 10257 (2015).
- Lee, J. H. et al. Wafer-scale growth of single-crystal monolayer graphene on reusable hydrogen-terminated germanium. Science 344, 286–289 (2014).
- Deng, B. et al. Wrinkle-free single-crystal graphene wafer grown on strain-engineered substrates. ACS Nano 11. 12337–12345 (2017).
- Burton, O. J., Massabuau, F. C. P., Veigang-Radulescu, V. P., Brennan, B., Pollard, A. J. & Hofmann, S. Integrated wafer scale growth of single crystal metal films and high quality graphene. ACS Nano 14, 13593–13601 (2020).
- Wang, M. et al. Single-crystal, large-area, fold-free monolayer graphene. Nature 596, 519–524 (2021).
- Deng, B. et al. Growth of ultraflat graphene with greatly enhanced mechanical properties. Nano Lett. 20, 6798–6806 (2020).
- Zhang, J. et al. Large-area synthesis of superclean graphene via selective etching of amorphous carbon with carbon dioxide. Angew. Chem. Int. Edn 58, 14446–14451 (2019).
- Liu, X. et al. The role of Cu crystallographic orientations towards growing superclean graphene on meter-sized scale. Nano Res. 15, 3775–3780 (2022).
- Hao, Y. et al. The role of surface oxygen in the growth of large single-crystal graphene on copper. Science 342, 720–723 (2013).
- Guo, W. et al. Oxidative-etching-assisted synthesis of centimeter-sized single-crystalline graphene. Adv. Mater. 28, 3152–3158 (2016).
- Lin, L. et al. Rapid growth of large single-crystalline graphene via second passivation and multistage carbon supply. Adv. Mater. 28, 4671–4677 (2016).
- Chuang, M. C. & Woon, W. Y. Nucleation and growth dynamics of graphene on oxygen exposed copper substrate. Carbon 103, 384–390 (2016).
- Choubak, S. et al. Graphene CVD: interplay between growth and etching on morphology and stacking by hydrogen and oxidizing impurities. J. Phys. Chem. C 118, 21532–21540 (2014).
- Choubak, S., Biron, M., Levesque, P. L., Martel, R. & Desjardins, P. No graphene etching in purified hydrogen. J. Phys. Chem. Lett. 4, 1100–1103 (2013).
- Dong, J., Zhang, L. & Ding, F. Kinetics of graphene and 2D materials growth. Adv. Mater. 31, 1801583 (2019).
- Zhang, W., Wu, P., Li, Z. & Yang, J. First-principles thermodynamics of graphene growth on Cu surfaces. J. Phys. Chem. C 115, 17782–17787 (2011).
- Yuan, S., Meng, L. & Wang, J. Greatly improved methane dehydrogenation via Ni adsorbed Cu(100) surface. J. Phys. Chem. C 117, 14796–14803 (2013).
- Mao, Z. & Campbell, C. T. Apparent activation energies in complex reaction mechanisms: a simple relationship via degrees of rate control. ACS Catal. 9, 9465–9473 (2019).
- Zhang, J. et al. New growth frontier: superclean graphene. ACS Nano 14, 10796–10803 (2020).
- Burton, O. J. et al. Putting high-index Cu on the map for high-yield, dry-transferred CVD graphene. ACS Nano 17, 1229–1238 (2022).
- Schmitz, M. et al. Fractional quantum Hall effect in CVD-grown graphene. 2D Mater. 7, 041007 (2020).
- Cançado, L. G. et al. Quantifying defects in graphene via Raman spectroscopy at different excitation energies. Nano Lett. 11, 3190–3196 (2011).
- Wang, L. et al. One-dimensional electrical contact to a two-dimensional material. Science 342, 614–617 (2013).
- Pezzini, S., Mišeikis, V., Pace, S., Rossella, F., Watanabe, K., Taniguchi, T. & Coletti, C. High-quality electrical transport using scalable CVD graphene. 2D Mater. 7, 041003 (2020).
- Zeng, Y. et al. High-quality magnetotransport in graphene using the edge-free Corbino geometry. Phys. Rev. Lett. 122, 137701 (2019).
- Polshyn, H. et al. Quantitative transport measurements of fractional quantum Hall energy gaps in edgeless graphene devices. Phys. Rev. Lett. 121, 226801 (2018).
- Li, X. et al. Large-area graphene single crystals grown by low-pressure chemical vapor deposition of methane on copper. J. Am. Chem. Soc. 133, 2816–2819 (2011).
- Banszerus, L. et al. Ultrahigh-mobility graphene devices from chemical vapor deposition on reusable copper. Sci. Adv. 1, e1500222 (2015).
- Luo, D. et al. The wet-oxidation of a Cu(111) foil coated by single crystal graphene. Adv. Mater. 33, 2102697 (2021).

Publisher's note Springer Nature remains neutral with regard to jurisdictional claims in published maps and institutional affiliations.

Springer Nature or its licensor (e.g. a society or other partner) holds exclusive rights to this article under a publishing agreement with the author(s) or other rightsholder(s); author self-archiving of the accepted manuscript version of this article is solely governed by the terms of such publishing agreement and applicable law.

© The Author(s), under exclusive licence to Springer Nature Limited 2024

Methods

Polycrystalline Cu(100) foil preparation

Polycrystalline Cu foils (Alfa Aesar Cu foil, 0.025 mm thick, 46365) were electropolished to a thickness of 15 μ m with a voltage bias of 2.04 V controlled by a potentiostat with a three-electrode setup, at a rotation speed of 15 Hz by the rotating disc method in phosphoric acid³⁹ (85 wt% in H₂O, Sigma-Aldrich W290017). The foils were first flushed with a large quantity of deionized (DI) water to remove residual acid and then rinsed three times in DI water and dried with N₂.

Single-crystal Cu(111) thin-film epitaxy on sapphire

Epi-polished 50.8-mm sapphire wafers diced along the c-plane (AdValue Technology SS-1WCF-2-50) were first cleaned by annealing at 1,000 °C for 12 h in a pure oxygen atmosphere, following previous reports 12 . Each wafer was immediately loaded into a magnetron sputtering system (AJA Orion 3) until base vacuum was achieved (1 × 10 $^{-8}$ Torr), and a 1,000-nm-thick Cu film was deposited with the following conditions: RF power 125 W, deposition rate 0.23 nm s $^{-1}$, argon partial pressure of 4 mTorr, substrate rotation speed of 0.67 Hz and chamber temperature of 20 °C. The wafer was then left in the chamber overnight to cool. To promote Cu recrystallization, each wafer was then annealed at 1,025 °C with 50 sccm Ar and 50 sccm H $_2$ at atmospheric pressure for 1 h with rapid cooling. Each Cu(111)/sapphire wafer was diced into 6-mm × 6-mm squares.

OF-CVD system design

The OF-CVD graphene system consists of a tube furnace (Lindberg/Blue M Mini-Mite Tube Furnace) with a 25.4-mm outer diameter quartz tube (Technical Glass Products). A smaller (22.86 mm outer diameter) tube is used to hold growth substrates. Gas cylinders are connected by means of Diameter Index Safety System (DISS) adapters with nickel gaskets. All gas tubing is electropolished stainless steel with VCR fittings (Stainless Design Concepts). Each purifier (SAES MicroTorr) and mass flow controller (Brooks GF Series) was specified for the target gas flow. The overall system pressure for each process was controlled with an exhaust throttling valve (MKS 253B-20-40-1). The main-chamber base pressure is measured with a cold cathode gauge (MKS 974B QuadMag), whereas the active process pressure is read by a capacitance manometer (MKS 627H21TBC1B). The synthesis process is automated to minimize human error and increase reproducibility. All trace-gas species (<100 AMU) within the OF-CVD reactor are monitored with using a residual gas analyser (SRS RGA 100).

When the OF-CVD main chamber requires venting for periodic maintenance, all vacuum piping and junctions are baked under vacuum at 150 °C for 24 h. After the bake, the entire length of the quartz tube is annealed at 1,090 °C under $\rm H_2$ flow. To minimize growth-chamber contamination, each substrate was placed in a quartz boat and loaded into a home-built load-lock apparatus. During sample loading, the load-lock chamber was kept at a positive pressure with a constant $\rm N_2$ flow to minimize exposure to ambient air. The load lock was pumped to a cross-over pressure of 5×10^{-6} Torr and the main chamber was pumped to 2×10^{-6} Torr before graphene growth.

OF-CVD graphene growth

The furnace was first heated to 500 °C in 100 mTorr H_2 (ULSI 6N) and held for 30 min (t_{anneal}) for sample annealing. The temperature was then ramped to the specified growth temperature (T_g) with 100 mTorr H_2 and held for 10 min (t_{stab}) for a stabilization period. H_2 flow was then cut off and the chamber purged with argon (ULSI 6N, 650 mTorr) for 1 min (t_{purge}). Next, argon flow was cut off and 5% CH₄ (ULSI 6N) diluted in argon (ULSI 6N) was introduced into the growth chamber for the specified growth time (t_g). Argon has a negligible effect on growth and nucleation (Supplementary Fig. 10). For experiments incorporating oxygen, 10×10^{-6} (ULSI 6N) diluted in argon was introduced during the

growth stage. Finally, methane flow was cut off and a linear actuator quickly moved the furnace away from the growth region, facilitating rapid cooling to room temperature ($t_{cool} \approx 30$ min) under 600 mTorr H₂. A visual representation of the typical OF-CVD graphene synthesis process is shown in Supplementary Fig. 2.

Graphene transfer

Gr/Cu foil wet transfer on Si⁺⁺/SiO₂. The Cu foil was first mounted to a glass slide on all sides with polymide tape before polymer spinning. A thin layer of poly (methyl methacrylate) (PMMA; 495 PMMA A4 from Kayaku, rotation speed 66.67 Hz, 1 min, bake at 140 °C, 2 min) was spun followed by a thick layer of paraffin using methods modified from ref. 40. First, the paraffin pellets (Sigma Aldrich #18634) were heated at 110 °C, whereas the PMMA-covered sample was heated to 50 °C to prevent paraffin solidification. Then the paraffin was quickly spun at a rotation speed of 16.67 Hz for 10 s without further baking. The sample was then mounted onto a glass slide on all sides with polymide tape with the polymer side facing down. The backside graphene was removed with 1 min of O₂ plasma at 100 W. The sample was then floated on top of APS-100 copper etchant (Transene) until the Cu was completely etched. The sample was rinsed with DI water five times and transferred to a hexamethyldisilazane (HMDS)-treated Si⁺⁺/SiO₂ substrate (oxide thickness 285 nm). The HMDS treatment along with the stiff paraffin layer were crucial steps to avoid trapped water in the Gr/SiO_2 interface. The sample was left to dry for 24 h at room temperature. The sample was submerged to acetone to remove the PMMA layer, thus lifting off the entire paraffin layer. Finally, the sample was rinsed with isopropyl alcohol IPA and dried with N2.

Gr/Cu(111) wet transfer on Si^{++}/SiO_2 . The Gr/Cu(111) film was first mounted onto a glass slide on all sides with polymide tape before polymer spinning. A thin layer of PMMA (495 PMMA A4 from Kayaku, rotation speed 66.67 Hz, 1 min, bake at 140 °C, 2 min) was spun. The sample was then submerged in a watch glass containing APS-100 copper etchant until the Cu was completely etched, allowing the PMMA/Gr to float to the liquid surface. The sample was rinsed with DI water five times and transferred to a HMDS-treated Si^{++}/SiO_2 substrate. The sample was left to dry for 24 h at room temperature. The sample was submerged in acetone to remove the PMMA. Finally, the sample was rinsed with IPA and dried with N_2 .

Gr/Cu(111) wet transfer on holey carbon grids. The preparation of suspended graphene sample is performed using a IPA-assisted method reported recently ⁴¹. A holey carbon grid (Quantifoil coated with 50-nm Au) was adhered to the Gr surface using 1 μ l of IPA as a sealant. This process increased the yield of the transferred graphene. The Cu etching and rinsing process was the same as the aforementioned transfer onto Si⁺⁺/SiO₂. After DI rinsing, the sample was dipped in IPA and dried naturally in ambient conditions.

Gr/Cu(111) dry transfer for h-BN encapsulation. The Gr/Cu(111) film was first placed into a humidity-controlled environment to promote formation of Cu_2O within the Gr/Cu(111) interface 38 . The sample was left in an oven at 75 °C for 12 h to fully oxidize the interface (Supplementary Fig. 25). Polydimethylsiloxane (PDMS) for the glass transfer slides was prepared from SYLGARD 184 by mixing ten parts base and one part curing agent. The PDMS was then mixed well and placed in a vacuum desiccator for bubble reduction. The resulting mixture was poured into a plastic Petri dish and cured at 60 °C for 48 h. To create a glass slide for transferring h-BN onto the graphene surface, PDMS was cut into a 2 mm × 2 mm square and gently mounted onto a glass slide. A liquid PDMS drop was introduced onto the square with curing at 60 °C for 2 h to impose the top surface with a larger curvature to finely control layer-by-layer pickup. A polypropylene carbonate (PPC) layer was spun on top of a bare silicon wafer, released with a

Article

hole-punched Scotch tape and then transferred to the PDMS surface. The final PPC/PDMS slide was heated at $100\,^{\circ}$ C for $5\,$ min to flatten the top surface.

After picking up the h-BN, the h-BN/PPC/PDMS stamp was brought into contact with the graphene surface at about 45 °C to peel up from the Cu₂O (polymer-free method used in Fig. 4d–j) or the SiO₂ (polymer-assisted method used in Fig. 3d) surface. The graphene was then encapsulated with another h-BN flake (for the graphite-gated device, a final layer of graphite with thickness approximately 10 nm was picked up subsequent to the bottom h-BN flake) and the PPC film was released at 120 °C on the target substrate. The PPC was then removed with room-temperature acetone for 1 h.

Graphene characterization

AFM measurements were performed using a Park FX40 AFM system in tapping/NCM mode with SSS-NCHR probes (NANOSENSORS). Measurements were performed at room temperature (300 K).

STM measurements were performed using a commercial Omicron ultra-high-vacuum STM system. Epitaxial graphene on Cu(111) samples were mounted onto metallic sample holders using a vacuum-safe silver paste (EPO-TEK H20E). Samples were then transferred into the STM chamber. A chemically etched tungsten STM tip was conditioned and calibrated on an Au(111) single crystal before the measurements. Measurements were performed at room temperature (300 K).

Electron backscatter diffraction (EBSD) measurements were performed using a Zeiss Sigma VP scanning electron microscope with a EDAX Hikari Plus detector. Grain orientation data were collected with 20 kV acceleration voltage.

Raman characterization of Gr/SiO₂ and graphene suspended on holey carbon grids were performed using a commercial Renishaw inVia Raman spectrometer with 532-nm excitation and collection in a 180° back-scatter geometry (1,800 lines per mm grating). All Raman mapping for Gr/SiO₂ used a 50× objective (0.75 numerical aperture). Spectral map parameters for 7 μm × 7 μm area Gr/SiO₂ (Fig. 3c) were 1 mW power, 1 s and one accumulation at 0.1 µm step size (N = 4,900). Spectral analysis for suspended graphene (Fig. 4c) used a 100× objective (0.85 numerical aperture) with the following parameters: 0.7 mW power, 120 s and 15 accumulations. Spectral map parameters for 40 μm × 40 μm area Gr/SiO₂ (synthesis on Cu foil) (Supplementary Fig. 18a-d) was with 1 mW power, 1 s and one accumulation at 0.3 μ m step size (N = 17.161). Spectral map parameters for 40 μm × 40 μm area Gr/SiO₂ (synthesis on Cu(111) film) (Supplementary Fig. 26d-f) were 1 mW power, 1 s and one accumulation at $0.25 \,\mu m$ step size (N = 26,896). Measurements were performed under ambient conditions.

Raman mapping of Gr/Cu and h-BN-encapsulated Gr was performed using a commercial HORIBA LabRam HR Evolution confocal microscope with 473-nm excitation and collection in a 180° back-scatter geometry (1,800 lines per mmgrating, 100 μ m confocal hole) through a $100\times$ objective (0.9 numerical aperture). Spectral map parameters for 20 μ m \times 20 μ m area Gr/Cu(111) (Supplementary Fig. 26a–c) were 1 mW power, 60 s and two accumulations at 1 μ m step size (N = 441). For the 3 μ m \times 3 μ m h-BN-encapsulated graphene (Supplementary Fig. 26g–i), the map was collected with 0.6 mW power, 20 s and two accumulations at a step size of 0.1 μ m (N = 1,380). All measurements were performed under ambient conditions.

XPS was performed using a Kratos Axis Ultra system with a monochromatic Al K α (1,486.7 eV) excitation source operating at 15 kV and 10 mA. Samples were pumped to a base pressure of at least 3.0 × 10⁻⁹ Torr (4.0 × 10⁻⁷ Pa). Kinetic energies of ejected electrons were measured with a hemispherical energy analyser located at a photoelectron take-off angle of 90° to the surface. A pass energy of 20 eV was used. Binding energies were normalized to Cu 2p from the copper substrate. We conducted data analysis with Shirley backgrounds in CasaXPS fitting to Voigt functions.

Device fabrication

For each lithography step, a bilayer resist consisted of copolymer (MMA (8.5) MAA EL10 from Kayaku, rotation speed 66.67 Hz, 1 min, bake at 150 °C, 2 min) and PMMA (950 PMMA A2 from Kayaku, rotation speed 66.67 Hz, 1 min, bake at 150 °C, 2 min). Each PMMA/MMA mask was first patterned by means of electron beam lithography (NanoBeam nB4). The Hall bar geometries for Gr-Si⁺⁺/SiO₂ devices were etched using O₂ plasma (60 sccm) with 30 W RF power and 40 mTorr process gas pressure in an inductively coupled plasma reactive ion etching (ICP-RIE) system (Oxford Plasmalab 100). The h-BN-encapsulated devices were etched with the edge-contact method 32 using CHF $_3$:O $_2$ (40:4 sccm) gas mixture with 10 W RF power and 40 mTorr process gas pressure in the same RIE system. Metal electrodes for all devices were deposited using electron-beam evaporation (Angstrom Engineering Nexdep) consisting of Cr/Pd/Au (2 nm/20 nm/60 nm).

Electrical characterization

The Gr-Si⁺/SiO₂ devices were measured at room temperature in a vacuum probe station (Lake Shore Cryotronics model FWPX) using a semiconductor device analyser (Keysight Technologies B1500A).

The h-BN-encapsulated samples were measured in a 3 He cryostat with a base temperature of 300 mK with a superconducting magnet up to 15 T. Four-terminal resistance measurements were carried out using a low-frequency lock-in technique at a frequency of 17 Hz. The carrier density was tuned by applying voltage on the Si⁺⁺/SiO₂ or few-layer-graphene gate with a DC source meter (Yokogawa). Further details on measurement configurations and geometry corrections for the h-BN-encapsulated sample can be found in Supplementary Figs. 28 and 29.

Data availability

Experimental data relevant to figures in the main text and data of numerical calculations are available at https://doi.org/10.5281/zenodo.10957342⁴². All other raw data are available from the corresponding author on request.

- Vidal, R. & West, A. C. Copper electropolishing in concentrated phosphoric acid: II. Theoretical interpretation. J. Electrochem. Soc. 142, 2689–2694 (1995).
- 40. Leong, W. S. et al. Paraffin-enabled graphene transfer. Nat. Commun. 10, 867 (2019).
- Zheng, L. et al. Uniform thin ice on ultraflat graphene for high-resolution cryo-EM. Nat. Methods 20, 123–130 (2023).
- 42. Amontree, J. et al. Source data for: Reproducible graphene synthesis by oxygen-free chemical vapour deposition. Zenodo https://doi.org/10.5281/zenodo.10957342 (2024).

Acknowledgements This work was primarily supported by the NSF MRSEC programme at Columbia through the Center for Precision-Assembled Quantum Materials (DMR-2011738). Magnetotransport studies were supported by the Department of Energy (DE-SC0016703). J.A. acknowledges support from NASA STRF (80NSSC19K1180). C.R.D. and J.H. acknowledge further support from the Gordon and Betty Moore Foundation's EPiQS Initiative, grant GBMF10277. R.M. and P.L.L. acknowledge support by the Canada Research Chair and the Natural Sciences and Engineering Research Council of Canada (grants nos. RGPIN-2019-06545 and RGPAS-2019-00050). Synthesis of boron nitride (K.W. and T.T.) was supported by the Elemental Strategy Initiative conducted by the MEXT, Japan (grant no. JPMXP0112101001) and JSPS KAKENHI (grant nos. JP19H05790 and JP20H00354), Analysis of Raman spectra (C.E.W.-S.) was supported by the National Science Foundation through the Howard-Columbia Partnership for Research and Education in Superatomic and 2D Materials (PRES2M) (DMR-2122151). Development of techniques for graphene transfer was supported by Hyundai Motor Company and the National Institute of Standards and Technology (NIST) (60NANB21D178). Certain commercial equipment, instruments or materials are identified in this manuscript to specify the experimental procedure adequately. Such identification is not intended to imply recommendation or endorsement by the NIST, nor is it intended to imply that the materials or equipment are necessarily the best available for the purpose. We would like to thank the following students for their contributions to set the stage for this project: E. Yanev for system design/installation and substrate optimization, N. Guillomaitre for substrate optimization and graphene synthesis process automation. A. Santimetaneedol for substrate optimization and process automation and A. Vera for analysis on the impact of copper morphology on graphene growth kinetics.

Author contributions J.A., X.Y., C.S.D. and J.H. conceived the experiments. J.H. supervised the project. J.A. and X.Y. performed the OF-CVD graphene growths. X.Y. prepared the electropolished Cu foils. J.A. and X.Y. prepared the Cu(111)/sapphire samples. T.A., J.A., X.Y.,

C.E.W.-S. and A.R.H.W. were responsible for Raman spectroscopy. X.Y. was responsible for AFM. M.H. was responsible for STM. A.J.B. was responsible for XPS. X.Y. and J.A. were responsible for EBSD. J.A. and X.Y. were responsible for wet graphene transfer. X.Y. prepared the suspended graphene samples. K.W. and T.T. supplied the h-BN. J.A. fabricated the OF-CVD graphene transport devices and J.A., J.P. and D.S. measured the devices. Z.W. and X.Y. fabricated and measured the exfoliated graphene transport devices. X.Y., K.B., R.M. and J.H. derived the growth kinetics model. J.A., X.Y. and C.C. were responsible for data analysis. C.S.D., X.Y., J.A. and P.L.L. designed and constructed the OF-CVD system. P.L.L. provided the comparative graphene sample from Infinite Potential Laboratories. C.S.D. and P.L.L. contributed theoretical discussion and guidance. J.H., J.A. and X.Y. drafted the manuscript and R.M., K.B., T.A. and A.R.H.W. revised it. All co-authors commented on the manuscript before its submission.

Competing interests Two of the authors (P.L.L. and R.M.) are inventors on US Patent 11447391. One author (C.S.D.) is founder of a company (Sindri Materials) seeking to commercialize advances in graphene synthesis.

Additional information

 $\textbf{Supplementary information} \ The online version contains supplementary material available at \ https://doi.org/10.1038/s41586-024-07454-5.$

Correspondence and requests for materials should be addressed to Katayun Barmak, Richard Martel or James Hone.

Peer review information *Nature* thanks Byung Hee Hong, Jeehwan Kim and the other, anonymous, reviewer(s) for their contribution to the peer review of this work.

Reprints and permissions information is available at http://www.nature.com/reprints.